SAND2018-12912J

Thermochemistry of the Smallest QOOH Radical from the Roaming Fragmentation of Energy Selected Methyl Hydroperoxide Ions

Kyle J. Covert,[a] Krisztina Voronova,[a] Krisztián G. Torma,[a] Andras Bodi,[b] Judit Zádor,[c,*] Bálint Sztáray[a,*]

[a]Department of Chemistry, University of the Pacific, Stockton, California, USA

[b]Laboratory of Synchrotron Radiation and Femtochemistry, Paul Scherrer Institute, Villigen, Switzerland

[c]Combustion Research Facility, Sandia National Laboratories, Livermore, California, USA

Table of Contents Entry

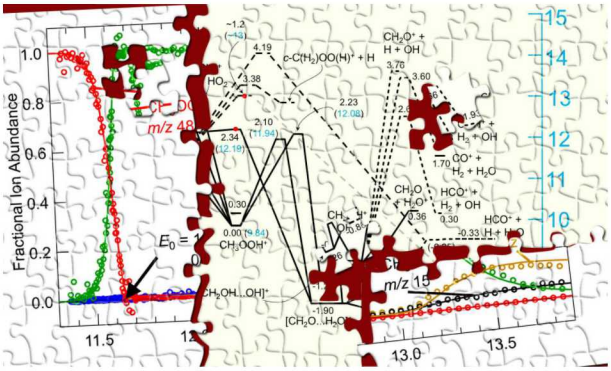

PEPICO spectroscopy and quantum-chemical calculations, including BOMD simulations, reveal the importance of dynamic effects in methyl hydroperoxide dissociative photoionization.

*Corresponding authors. E-mail: jzador@sandia.gov and bsztaray@pacific.edu.

Abstract

The dissociative photoionization processes of methyl hydroperoxide (CH_3OOH) have been studied by imaging Photoelectron Photoion Coincidence (iPEPICO) spectroscopy experiments as well as quantum-chemical and statistical rate calculations. Energy selected CH_3OOH^+ ions dissociate into CH_2OOH^+, HCO^+, CH_3^+, and H_3O^+ ions in the 11.4–14.0 eV photon energy range. The lowest-energy dissociation channel is the formation of the cation of the smallest "QOOH" radical, CH_2OOH^+. An extended RRKM model fitted to the experimental data yields a 0 K appearance energy of 11.647 ± 0.005 eV for the CH_2OOH^+ ion, and a 74.2 ± 2.6 kJ mol^{-1} mixed experimental-theoretical 0 K heat of formation for the CH_2OOH radical. The proton affinity of the Criegee intermediate, CH_2OO, was also obtained from the heat of formation of CH_2OOH^+ (792.8 ± 0.9 kJ mol^{-1}) to be 847.7 ± 1.1 kJ mol^{-1}, reducing the uncertainty of the previously available computational value by a factor of 4. RRKM modeling of the complex web of possible rearrangement-dissociation processes were used to model the higher-energy fragmentation. Supported by Born–Oppenheimer molecular dynamics simulations, we found that the HCO^+ fragment ion is produced through a roaming transition state followed by a low barrier. H_3O^+ is formed in a consecutive process from the CH_2OOH^+ fragment ion, while direct C–O fission of the molecular ion leads to the methyl cation.

Introduction

Methyl hydroperoxide (MHP), CH_3OOH, the simplest organic hydroperoxide, plays an important role in combustion[1, 2] and atmospheric chemistry.[3] MHP is formed when OH radicals react with CH_3O (methoxy radical): Jasper *et al.*[2] have shown that MHP is the major product in the 1–10^5 Torr pressure range, up to ca. 1500 K. MHP is also formed when CH_3OO reacts with molecules

and radicals with easily abstractable hydrogen atoms, such as HO_2, H_2O_2, or CH_3O. MHP, like other organic hydroperoxides, is relatively unstable and easily decomposes thermally or photolytically, yielding radical or molecular fragments.[2, 4] The other main loss route for MHP in an oxidative environment is through bimolecular reactions, primarily with OH,[5] forming mostly CH_3OO. However, when MHP reacts with Cl atoms, it forms mostly CH_2OOH,[6] the smallest hydroperoxyalkyl radical, generally termed as QOOH. These short-lived carbon-centered radicals can also be formed from the corresponding alkylperoxy radicals (ROO) via internal hydrogen abstraction for $C_{n \geq 2}$, and play a central role in autooxidation processes.[1, 7, 8] Longer-chain QOOH radicals are important in propagation and branching steps of radical chain reactions and are central in low-temperature autoignition combustion chemistry.[1] They are also unstable and decompose rapidly to form cyclic ethers + OH or alkenes + HO_2, or react quickly with O_2 and contribute to radical chain branching. The most unstable QOOH radicals are the ones where both the radical site and the OOH group are on the same carbon atom. These radicals, *e.g.,* CH_2OOH, fall apart to a carbonyl and OH. So far, only one QOOH radical has been detected directly, the resonance stabilized 2-hydroperoxy-4,6-cycloheptadienyl,[8] with the kinetics of another one characterized directly.[7] There is no experimental thermodynamic data available for any QOOH in the literature.

To establish reliable thermochemistry for its fragments, the ionization energy (IE) and the heat of formation ($\Delta_f H^\circ$) of MHP are crucial as thermochemical anchor values and future studies involving more complex organic hydroperoxides will also benefit from such anchors. Matthews derived the 0 K MHP $\Delta_f H^\circ$ as -113 ± 4 kJ mol^{-1} in the gas phase from the O–O bond dissociation energy and the heats of formation of the formed fragments.[9] Based on Khursan and Martem'yanov's work,[10] Komissarov reported a heat of formation of –131.0 kJ mol^{-1} at 298 K,

which converts to –118.2 kJ mol^{-1} at 0 K, while the Active Thermochemical Tables (ATcT, version 1.122)[11] value is –114.90 ± 0.74 kJ mol^{-1} at 0 K.

Using a positive ion thermochemical cycle is often one of the most accurate ways to derive experimental thermochemical data on elusive gas-phase species. These cycles generally include the ionization energy of the stable parent molecule, which in case of MHP was measured as 9.87 eV by Yi-Min *et al.*[12] using He-I photoelectron spectroscopy (PES). The IE can also be calculated using the ATcT heat of formation of the MHP^+ cation, 832.3 ± 2.5 kJ mol^{-1}, to be 9.82 ± 0.03 eV. There have been studies published on the dissociation of protonated alkyl hydroperoxides,[13, 14] but there is a lack of data on the fragmentation dynamics of relatively low-energy molecules formed in single-photon excitation or ionization, the type of experiments most useful for deriving accurate thermochemical information. In particular, threshold photoelectron photoion coincidence spectroscopy (TPEPICO) is extremely well suited to determine very accurate dissociative photoionization energies and to explore the dissociation mechanisms of internal energy-selected gas phase ions.[15-20] The goals of this work are to derive thermochemical data on the smallest QOOH species, CH_2OOH, and to understand the CH_3OOH^+ ion decomposition dynamics by imaging PEPICO (iPEPICO) experiments and *ab initio* quantum chemical calculations.

Experimental

1. Methyl hydroperoxide synthesis

MHP was synthesized by a nucleophilic addition reaction between dimethyl sulfate (DMS) and hydrogen peroxide (H_2O_2, 30%), in the presence of potassium hydroxide (KOH):[21]

$$(CH_3)_2SO_4 + 2\ H_2O_2 + 2\ KOH \rightarrow 2\ CH_3OOH + 2\ H_2O + K_2SO_4$$

All reagents were purchased from Sigma–Aldrich and used without further purification. DMS (77 g) and H_2O_2 (115 mL) were mixed in a 250 mL round bottom flask. The flask was submerged in

an ice bath (0 °C) to keep the reaction temperature below 20 °C, while an aqueous KOH solution (40% w/v) was added dropwise. The byproduct, dimethyl peroxide, escaped as a gas. After the reaction came to completion, sulfuric acid (H_2SO_4, 98%) was added at 0 °C to acidify the reaction mixture to pH = 6. The formed K_2SO_4 precipitate was removed by filtration. Then, the solution was extracted with anhydrous diethyl ether and dried over $MgSO_4$. The product was fractionally distilled at 50 °C under vacuum (80 Torr). The purity of MHP (≈98%) was confirmed by the photoionization mass spectra in the iPEPICO experiment.

2. Imaging PEPICO experiments

The experiments were carried out on the iPEPICO endstation of the X04DB bending magnet VUV beamline at the Swiss Light Source within the Paul Scherrer Institut in Switzerland.[22] A detailed description of the spectrometer is given elsewhere.[23] Briefly, gas-phase molecules are photoionized using tunable vacuum ultraviolet (VUV) synchrotron radiation and the resulting photoions and photoelectrons are detected in coincidence. The kinetic energy of the photoelectrons is analyzed by velocity map imaging (VMI) while the photoions are mass-analyzed by their time of flight (TOF), using a Wiley–McLaren setup.[24] The energetics of ionic dissociation processes is measured by scanning the ionizing photon energy and energy-selecting the photoions by measuring coincidences with only threshold (*i.e.* originally close to zero kinetic energy) electrons. Accurate dissociative photoionization onsets are best determined by recording and modeling the fractional ion abundances as a function of the photon energy, referred to as the breakdown diagram.

The liquid MHP sample was placed in a glass vial at room temperature and the sample vapor was introduced into the iPEPICO ionization region from the headspace through a 30 cm long Teflon tube. The pressure in the ionization chamber was kept between 1.1–3.6 × 10^{-6} mbar

during the experiments. The MHP sample was ionized within a 2 mm × 2 mm cross section by the incident VUV synchrotron radiation between 11.3 and 14.0 eV, after the higher harmonics were removed in a gas filter containing a mixture of Ne, Ar, and Kr. The photon energy was calibrated using the Ar and Ne 11s′–14s′ autoionization lines in grating 1st and 2nd order. The photon energy resolution was measured to be better than 3 meV. After the photoelectrons and photoions are extracted with a constant 80 V cm^{-1} electric field, the photoelectrons are velocity map imaged onto a Roentdek delay line detector, with an electron kinetic energy resolution better than 1 meV at threshold. The photoions were mass analyzed by a two-stage Wiley−McLaren TOF mass spectrometer with a 5.5 cm long extraction, a 1 cm long acceleration, and a 55 cm long drift region and detected by a Jordan TOF C-726 microchannel plate detector.

Photoelectron and photoion detection events serve as start and stop signals, respectively, in a multiple-start–multiple-stop coincidence data acquisition scheme.[25] Threshold electrons are detected in the center of the photoelectron VMI and the contribution of "hot" electrons is subtracted from the center signal, based upon the average count rate in a ring region surrounding the center. This method is conceptually simpler than slow photoelectron spectroscopy[26] or inverting the coincident images[27] and has been found to be a good approximation for the hot electron correction in the overwhelming majority of systems.[28] Furthermore, as the kinetic energy resolution is best in the center of the image, it also yields the best attainable energy resolution. Ion abundances are thus plotted by keeping only the coincidences with threshold photoelectrons.[29]

3. Theoretical methods

To characterize the CH_3OOH^+ potential energy surface (PES), we optimized stationary point geometries and calculated frequencies using the M06-2X/MG3S level of theory with 'Grid =

150974' and 'verytight' optimization parameters in Gaussian09,[30] and calculated single-point energies at the RCCSD(T)-F12b/cc-pVQZ-F12 level using the Molpro 2012 suite of programs.[31] We will refer to these energies as F12//M06-2X. The T1 diagnostics[32, 33] for some key species were above 0.025, but the agreement with the experiment in general suggests that the calculated energies are nevertheless accurate, perhaps due to the large basis set. In a few cases, calculations with the MG3S basis set (which is equivalent to 311G(2p) on H atoms and 6-311+G(2df) on C and O atoms), in combination with the M06-2X functional did not converge to a saddle point, although one was found with the other methods. In these cases, the geometry optimization and frequency calculations were done using one or more of these levels: M06-2X/6-311++G(d,p), B3LYP/6-311++G(d,p), MP2/6-311++G(d,p) in Gaussian, or CASPT2/aug-cc-pV*n*Z (*n* = D or T), as implemented in Molpro 2012.

The breakdown curves were modeled using the Rice–Ramsperger–Kassel–Marcus (RRKM) framework for the ionic dissociation reactions. Vibrational frequencies and rotational constants were used to calculate the thermal energy distribution of the neutral precursor molecules, as well as densities and numbers of states in the rate equation and to obtain the internal energy distribution of intermediate fragments based on statistical distribution of product internal energies. The unimolecular rate constant, $k(E)$, is calculated from the RRKM rate equation for each dissociation channel:

$$k(E) = \frac{\sigma N^{\ddagger}(E - E_0)}{h\rho(E)}$$

where E_0 is the dissociation threshold, $N^{\ddagger}(E - E_0)$ is the sum of states of the transition state up to energy $E - E_0$, $\rho(E)$ is the parent ion density of states, σ is the symmetry factor, and h is Planck's constant. For tight or fairly tight transition states, we applied RRKM theory within the rigid rotor and harmonic oscillator (RRHO) framework, which was refined with inclusion of torsional

anharmonicity and tunneling in 1-D through Eckart barriers. For these calculations, we used the MESS code to evaluate the state counts.[34] Some of the transition states are barrierless and for these cases, we applied variable-reaction-coordinate transition state theory[35, 36] (VRC-TST) to count states, as implemented in the VaReCoF code.[37]

In order to fit the experimental data, we assumed that the thermal internal energy distribution of CH_3OOH is shifted into the ion manifold faithfully in threshold photoionization, and varied model parameters, such as appearance energies and the lowest frequency vibrational modes, as outlined in Section 3 of Results and discussion. The latter was done by the Beyer-Swinehart-Stein-Rabinovitch (BSSR) anharmonic density count method[38] where the symmetric top rotational density of states were calculated classically, and the anharmonic state count for the hindered rotors (H–C–O–O and C–O–O–H) was obtained by solving the vibrational Schrödinger equation on a free rotor basis set.[39]

Moreover, Born–Oppenheimer molecular dynamics (BOMD) simulations[30] were performed (as implemented in Gaussian 09) to qualitatively investigate the importance of non-RRKM behavior of the dissociation channels beyond a roaming saddle point. The input velocities were calculated based on quasi-classical fixed normal mode sampling and the input geometry was selected as the saddle point of the isomerization TS. The calculation proceeded in 1 fs time steps, up to 1000 fs at the MP2/6-31+G(d) level. Excess energy above the barrier was specified as 0.1 and 1.0 eV to investigate the changes in dynamics with respect to energy in the system. An 8 Å threshold distance was used between fragments and atoms of the various dissociation paths as termination criterion for the calculations.

Results and discussion

1. Experimental breakdown curves

Threshold photoionization TOF mass spectra of energy-selected MHP^+ cations were measured in the 11.3–14.0 eV photon energy range. The area of each photoion's TOF peak was integrated and the fractional parent and fragment ion abundances were plotted as a function of photon energy in the breakdown diagram shown in Fig. 1. Below 11.4 eV, the only detected species is the MHP^+ parent ion at m/z = 48. Starting at 11.40 eV, the abundance of the parent ion begins to decrease as the hydrogen-loss m/z = 47 fragment ion appears, and the parent ion signal completely vanishes by 11.65 eV. From 12 eV, the m/z = 29 ion starts to appear and its ratio slowly increases throughout the rest of the investigated photon energy range. Since there is only one carbon atom in the parent molecule and double ionization is not possible in this energy range, m/z = 29 can only correspond to an HCO^+ or COH^+ ion. The next ion, m/z = 19 (H_3O^+) begins to appear at 12.55 eV as a trace species and its abundance quickly rises starting at 13.0 eV until it starts to decline at 13.5 eV. The last fragment ion observed is at m/z = 15 (CH_3^+). The methyl ion appears at 13.0 eV and its very slow rise clearly indicates a parallel channel from the MHP^+ molecular ion, similarly to the appearance of the m/z = 29 channel.[40]

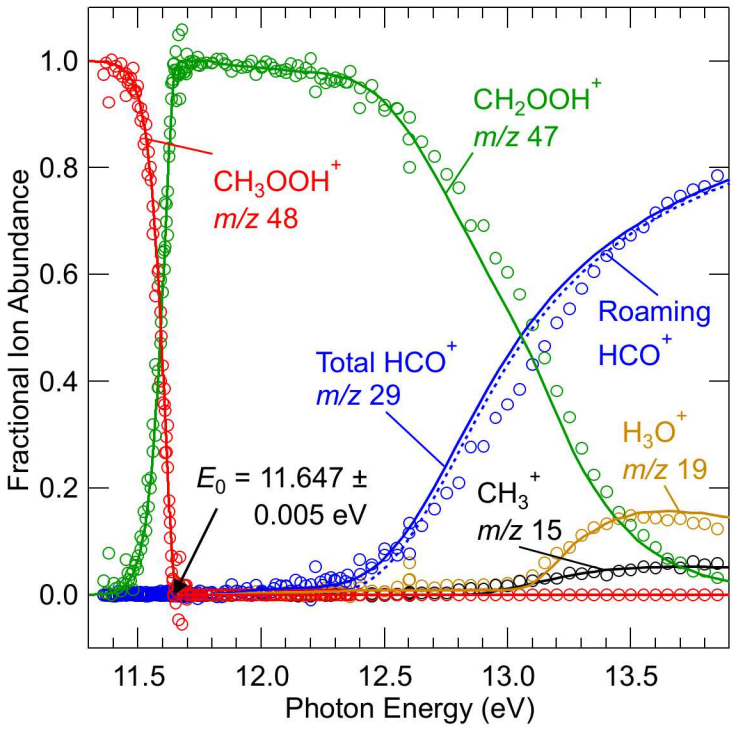

Figure 1. Open circles represent the experimental breakdown diagram of MHP in the 11.4–13.9 eV photon energy range. The adjusted RRKM model is shown with lines. The dotted blue line is the contribution of the roaming channel for the HCO^+ ion (almost 100%). For details of the theoretical results, see Section 3 of Results and discussion.

Contrastingly, the quicker rise of the *m/z* = 19 channel hints at a different mechanism for this dissociation process and suggests that it may be a secondary ion formation channel from CH_2OOH^+. However, as the abundance of its proposed parent ion (*m/z* = 47) is also changing, a simple visual inspection of the full breakdown curve is inadequate to state with certainty the origin of the *m/z* = 19 signal. Therefore, the pairwise fractional abundances (*i.e.* $\frac{I_{19}}{I_{19}+I_{47}}$) of the *m/z* = 19 vs. 47, and 29 vs. 47 ions are shown in Fig. 2, which illustrates that the two pairs exhibit markedly different behavior. The rise of the *m/z* = 29 ion does not show a clear break, rather a slow rise from

the background, typical of a parallel channel, while the *m/z* = 19 ion appears much more suddenly at 13 eV, indicating consecutive dissociation of the *m/z* = 47 ion.

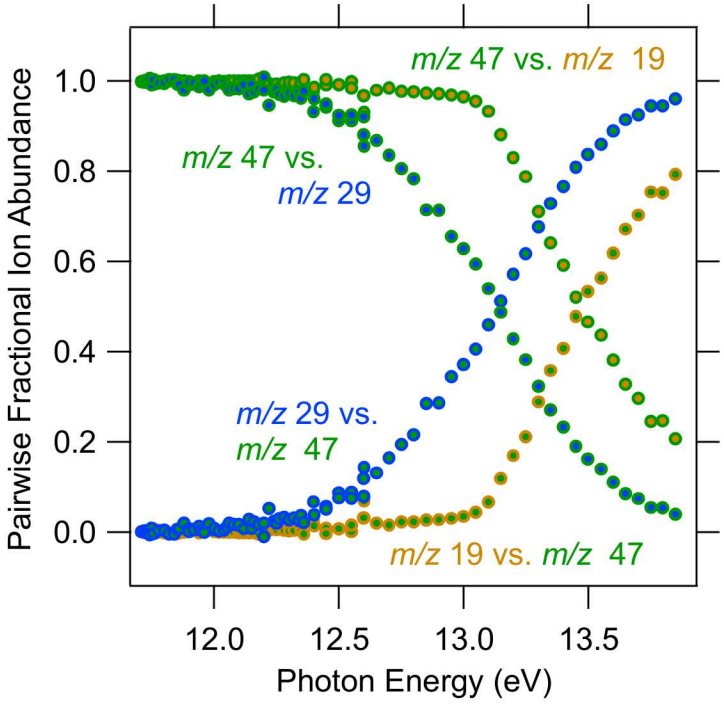

Figure 2. Pairwise fractional ion abundances for the *m/z* = 29 vs. 47 and *m/z* = 19 vs. 47 ions. The gradual rise exhibited by the first pair suggests parallel formation of these species, while the *m/z* = 19 ion is likely formed in a consecutive dissociation step from the *m/z* = 47 ion – apart from a small fraction that very gradually increases to a few percent in the 12–13 eV energy range.

2. Characterization of the CH_3OOH^+ PES

The CH_3OOH^+ radical cation can undergo a surprising number of possible dissociation and isomerization reactions as summarized in the schematic potential energy surface in Fig. 3. Fig. 4 shows the corresponding calculated ion structures and their energies, relative to the MHP^+ molecular ion.

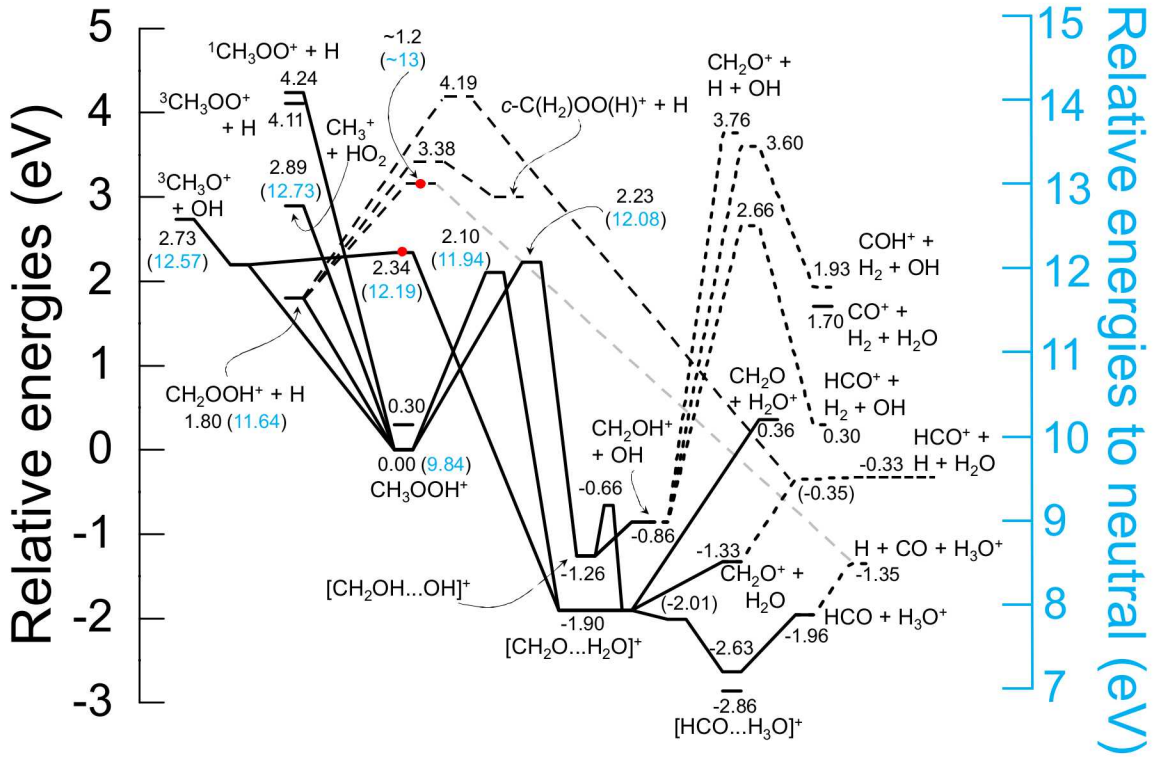

Figure 3. Calculated ZPE-corrected energies relative to CH_3OOH^+ at the RCCSD(T)-F12b/cc-PVQZ-F12//M06-2X/MG3S level of theory (left axis). The blue numbers in parentheses and the blue right-hand axis are energies relative to the neutral CH_3OOH. Dashed lines indicate secondary dissociation channels and the lighter dashed line indicates uncertainties about the exact mechanism after the saddle point. The red dots indicate roaming transition states.

The adiabatic ionization energy of CH_3OOH to the lowest CH_3OOH^+ conformer is 9.84 eV at the F12//M06-2X level (the T1 diagnostic is 0.031 for the cation, suggesting a perhaps slightly larger than usual uncertainty in its energy), which is within the confidence interval of the ATcT recommended value of 9.82 ± 0.03 eV, in good agreement with the 9.87 eV by Yi-Min *et al.*[12] The other conformer of CH_3OOH^+ is 0.30 eV higher in energy and differs in the dihedral angle of the

O–OH hindered rotor. As also suggested by the experiments, we found that CH_3OOH^+ can undergo the following simple bond scission reactions:

$$CH_3OOH^+ \rightarrow CH_2OOH^+ + H \qquad (1a)$$

$$\rightarrow {}^3CH_3O^+ + OH \qquad (1b)$$

$$\rightarrow CH_3^+ + HO_2 \qquad (1c)$$

$$\rightarrow {}^3CH_3OO^+ / {}^1CH_3OO^+ + H \qquad (1d)$$

In the following section, we discuss the key properties of each channel, while more details and figures are provided in the SI–2 part of the Supporting Information. The experimentally observed threshold for $CO_2H_3^+$ (m/z = 47, channel 1a) is 11.647 ± 0.005 eV, in very good agreement with the F12//M06-2X calculations for the CH_2OOH^+ fragment ion, 11.64 eV. The ZPE-exclusive energy profiles for channel 1a (Fig. SI–2.1) show that this reaction has a slightly submerged barrier, which is the dynamical bottleneck for dissociation at energies above the asymptote. The ZPE-corrected RCCSD(T)-F12b/cc-PVQZ-F12//CASPT2(3e,3o)/aug-cc-pVTZ energy of the barrier is 0.04 eV higher than the thermochemical limit but dissociation can proceed through tunneling already at the thermochemical threshold.

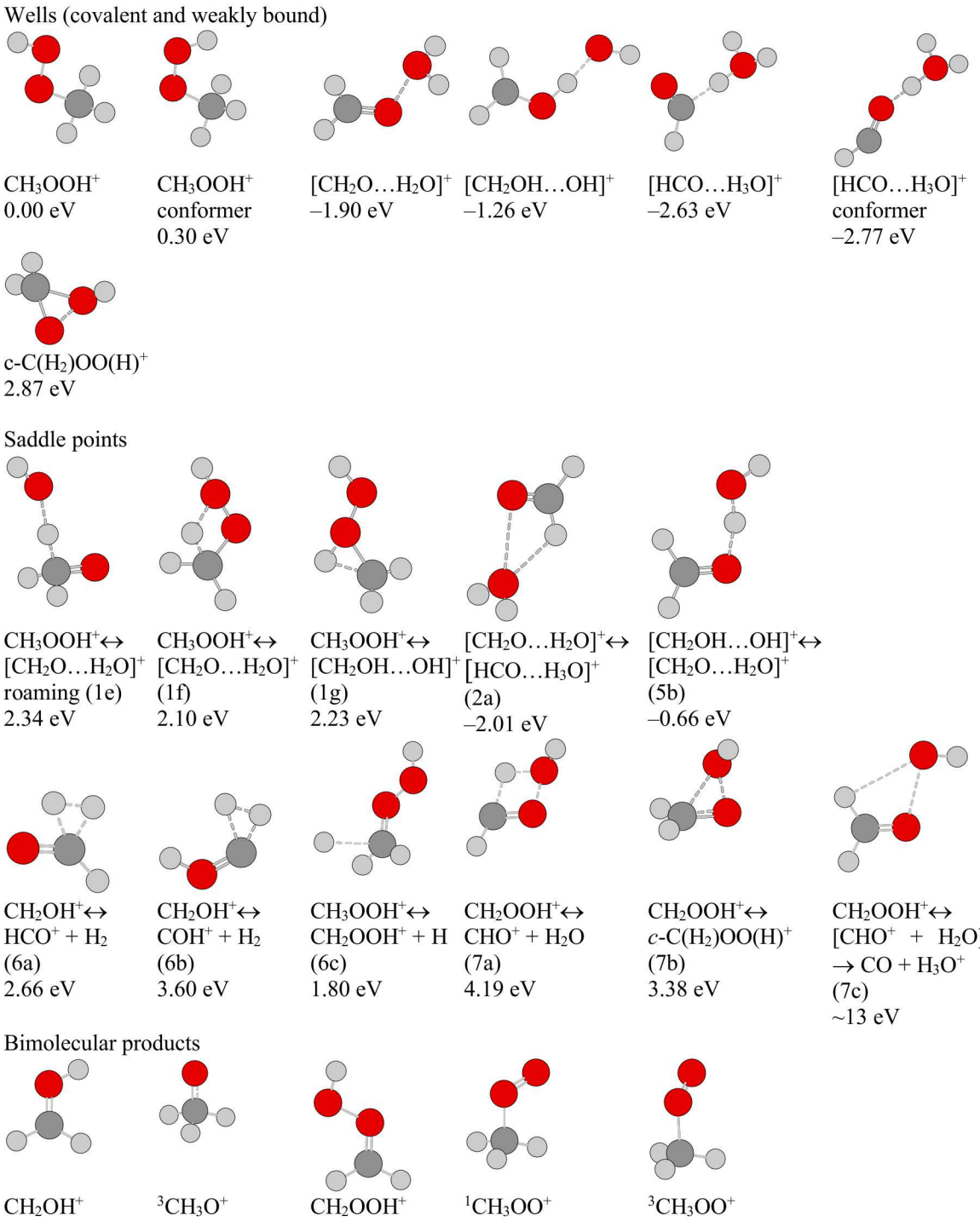

Figure 4. Structures of wells, saddle points, and bimolecular products. The Cartesian coordinates of the structures can be found in SI–1. Energies are relative to CH_3OOH^+.

When breaking the O–OH bond (channel 1b) at DFT levels, the calculated energy becomes oscillatory, likely due to wave function instabilities and high multireference character. CASPT2(3e,3o) calculations show that the product is $^3CH_3O^+$ (Fig. SI–2.2). The potential energy scan in A″ symmetry shows a flat region between 2.5 and 4.0 Å, which corresponds to the OH group interacting with the methyl end of the $^3CH_3O^+$ fragment through dipole-dipole and dipole-ion forces, forming a $[OCH_3\ldots OH]^+$ complex. Scanning the bond along a straight line (*i.e.*, keeping angles and dihedral in the C–O–O–H motif fixed) shows no such feature. The plateau observed in the relaxed scan is more than 0.5 eV below the asymptote, suggesting that roaming reactions can play an important role in this system. Searching for such processes, we have found a saddle point where the OH radical abstracts an H atom leading to another loosely attached complex $[CH_2O\ldots H_2O]^+$, which is 1.90 eV more stable than CH_3OOH^+ itself.

$$CH_3OOH^+ \rightarrow [CH_3O\ldots OH]^{+\ddagger} \rightarrow [CH_2O\ldots H_2O]^+ \qquad (1e)$$

We were able to locate this saddle point at the MP2/6-311++G(d,p) level of theory. The accurate barrier height is 2.34 eV above CH_3OOH^+, which means that it is 0.38 eV below the $^3CH_3O^+$ asymptote, making this a feasible roaming pathway and we will show that it is indeed responsible for the observed HCO^+ signal.

For the $CH_3^+ + HO_2$ channel (1c), we scanned the energy along the C–O bond and found no reverse barrier at the M06-2X/MG3S level of theory (Fig. SI–2.3). Note that $m/z = 15$ appears around 12.7 eV in the experiments, and the calculated threshold for 1c is 12.73 eV, suggesting that this is the most likely route to this fragment.

CH_3OOH^+ can also isomerize in two more ways via tight transition states. One of the H-atoms from the methyl group can transfer to the outer oxygen atom via a 2.10 eV barrier:

$CH_3OOH^+ \rightarrow [CH_2O\ldots H_2O]^+$ (1f)

Note that the product of this reaction is the same as that of 1e, but the corresponding saddle point geometry (see Fig. 4) and thus the low frequencies are very different for these two isomerization channels.

The other isomerization channel starting from CH_3OOH^+ involves a methyl H atom transferring to the inner O atom via a 2.23 eV barrier, resulting in another weakly bound complex:

$CH_3OOH^+ \rightarrow [CH_2OH\ldots OH]^+$ (1g)

The two weakly bound complexes, $[CH_2O\ldots H_2O]^+$ and $[CH_2OH\ldots OH]^+$, can undergo further reactions. The energetically most favorable pathway for $[CH_2O\ldots H_2O]^+$ is to transfer another H atom to the H_2O part, forming another weakly bound complex, $[HCO\ldots H_3O]^+$, in an essentially barrierless reaction:

$[CH_2O\ldots H_2O]^+ \rightarrow [HCO\ldots H_3O]^+$ (2a)

We were able to locate a saddle point 0.01 eV above the energy of the $[CH_2O\ldots H_2O]^+$ complex using M06-2X/MG3S, and we also confirmed its connectivity with IRC calculations, but this miniscule barrier disappears at the coupled cluster level. We also found another $[HCO\ldots H_3O]^+$ conformer lying at a somewhat lower energy, –2.86 eV relative to CH_3OOH^+, but it is not directly available from $[CH_2O\ldots H_2O]^+$.

The weak $[HCO\ldots H_3O]^+$ complex can dissociate in a barrierless reaction to form HCO and a hydronium ion, with a –1.96 eV asymptote, representing the most exothermic reaction channel.

$[HCO\ldots H_3O]^+ \rightarrow HCO + H_3O^+$ (3)

Aside from isomerization reactions, the formaldehyde–water ionic complex can also dissociate directly:

$$[CH_2O\ldots H_2O]^+ \rightarrow CH_2O^+ + H_2O \qquad (2b)$$

$$\rightarrow CH_2O + H_2O^+ \qquad (2c)$$

with the charge located on the formaldehyde being the much more favorable channel (–1.33 eV versus +0.36 eV relative to CH_3OOH^+). Once the two fragments depart, the formaldehyde ion can lose an H atom in a process that has a slight reverse barrier at M06-2X/MG3S, but the barrier disappears at the coupled cluster level:

$$CH_2O^+ \rightarrow HCO^+ + H \qquad (4)$$

Because the threshold energy to make $[CH_2O\ldots H_2O]^+$ is at least 2.10 eV, channels 2–4 are all open once the corresponding saddle point is surmounted. $[CH_2OH\ldots OH]^+$ can either lose a neutral OH in a barrierless reaction, or, can isomerize into $[CH_2O\ldots H_2O]^+$:

$$[CH_2OH\ldots OH]^+ \rightarrow CH_2OH^+ + OH \qquad (5a)$$

$$\rightarrow [CH_2O\ldots H_2O]^+ \qquad (5b)$$

The latter saddle point is a roaming-like internal H abstraction between the two parts of this weakly bound complex, but unlike in the previous case (1e), this saddle point is above the corresponding asymptote. The resulting CH_2OH^+ cation can further dissociate:

$$CH_2OH^+ \rightarrow HCO^+ + H_2 \qquad (6a)$$

$$\rightarrow COH^+ + H_2 \qquad (6b)$$

$$\rightarrow CH_2O^+ + H \qquad (6c)$$

The H atom loss (6c) shows no reverse barrier, while the other two channels have a high reverse barrier and all three have an activation energy higher than the controlling barrier at 2.23 eV, making these channels less, if at all, important for our investigations.

In search for a path to *m/z* = 19, we have also investigated the fragmentation of the dissociation products of CH_3OOH^+. Running our KinBot code[7, 41] on CH_2OOH^+ found two reactions with tight transition states:

$CH_2OOH^+ \rightarrow [CHO^+ \ldots H_2O]$ (7a)

$\rightarrow$ *c*-$C(H_2)OO(H)^+$ (7b)

Channel 7a could in principle produce H_3O^+, *i.e.*, *m/z* = 19 if the H_2O molecule abstracts a proton from CHO^+ before the fragments separate completely, however, the barrier for this reaction is above 4 eV relative to CH_3OOH^+, which is much higher than the experimental appearance energy of this fragment. The barrier for the cyclic compound (7b) is also slightly too high (3.38 eV above relative to CH_3OOH^+, and 13.23 eV relative to CH_3OOH) and we were not able to locate a forward pathway from this cyclic structure to H_3O^+. However, it is very likely that similar electronic structure problems plague the channels of the decomposition of this fragment as are observed when CH_3OOH^+ loses the OH moiety, indicated by large T1 diagnostics. Interestingly, we found that a singlet scan along the O–O bond of CH_2OOH^+ results in two fragments by simple bond fission, while assuming a triplet electronic structure yields a roaming-like pathway, where the OH abstracts one of the H atoms of the CH_2O^+ moiety:

$CH_2OOH^+ \rightarrow CHO^+ + H_2O$ (7c)

We used the geometries along the triplet path and calculated CASPT2(4e,4o)/aug-cc-pVTZ and CCSD(T)-F12b/cc-pVQZ-F12 energies, and found that both methods yield a barrier, which is an

encouraging agreement with the experimentally observed ≈13 eV rise of H_3O^+. (Note that the O–O distance at the saddle point for 7a is ≈1.5 Å, while it is ≈2.2 Å for 7c according to the CCSD(T)-F12b potential.) For these potential curves, see Fig. SI–2.4. We were not able to optimize to a saddle point in this roaming region with any of the methods, because of convergence problems (similarly to the observations of Ref. [42]) and, therefore, the computational evidence that the second H abstraction indeed happens after the first one is only circumstantial.

The other primary fragments have no obvious dissociation pathways that yield exothermic products. We also considered other possible products, such as $CO^+ + H_2 + H_2O$, which are also high in energy as shown in Fig. 3.

In summary, the most likely ions to be observed based on the calculated PES are CH_3OOH^+ (9.84 eV, m/z = 48), CH_2OOH^+ (11.64 eV, m/z = 47), H_3O^+ (11.94 eV and ~13 eV, m/z = 19), CH_2O^+ (11.94 eV, m/z = 30), HCO^+ (11.94 eV, m/z = 29), CH_2OH^+ (12.08 eV, m/z = 31), $^3CH_3O^+$ (12.57 eV, m/z = 31), and CH_3^+ (12.73 eV, m/z = 15), where the stated energies are the calculated dissociative photoionization thresholds relative to neutral CH_3OOH.

3. RRKM modeling of the breakdown curves

Based on the PES (Fig. 3), the fractional ion abundances were calculated as shown in Fig. 1 within the RRKM framework for the 1a, 1b, 1c, 1e, 1f, and 1g reactions and including the 300 K thermal distribution of the neutral CH_3OOH. In the case of a fast dissociation, ion abundances for the first daughter ion formation (in this case, 1a) simply reflect the room-temperature internal energy distribution of the neutral precursor, transposed to the ionic manifold by the ionizing photon. Ion abundances for parallel dissociation processes, which dominate the breakdown diagram above 12

eV, are determined by the fragmentation rate constant ratios, *i.e.*, the relative transition state numbers of states as a function of internal energy.

To calculate the transition state number-of-state functions, we used VRC-TST for channels 1a, 1b, and 1c. Furthermore, we also took into account both the outer (long-range) and inner (saddle point) regimes in a two-transition-state model for 1a.[43, 44] More details can be found in SI-2. A small number of parameters were varied in the RRKM fit to reproduce the experimental breakdown diagram: the lowest frequency of the roaming saddle point was changed from 50.4 to 12 cm^{-1} (corresponding to a loose OH rotor motion), the roaming barrier was decreased by 0.04 eV (4.2 kJ mol^{-1}), and the state count for the barrierless CH_3 channel was decreased by a factor of 2.3. As the state count was obtained by sampling the PES, this decrease is only akin to increasing a low-frequency mode by a factor of 2.3 for a tight transition state, but was brought about directly by scaling the state count and not indirectly by scaling a transitional frequency. As for the 0 K appearance energy of this channel, we have used the calculated thermochemical limit (12.73 eV, see Figure 3). While the experimental breakdown curve hints at a possible earlier onset for methyl cation formation, the very low ion abundances do not allow for a more reliable experimental estimate. Furthermore, the RCCSD(T)-F12b/cc-PVQZ-F12//M06-2X/MG3S calculated E_0 of 12.73 eV is in very good agreement with the ATcT ($CH_3^+ + HO_2 - CH_3OOH$) enthalpy difference of 12.741 ± 0.008 eV. Furthermore, the best fit to the slow decay of m/z = 47 and the slow rise of m/z = 29 above in the experimental breakdown curves was provided by decreasing the barrier for the tight transition state of channel 1f by 0.17 eV (16.7 kJ mol^{-1}. In the model, we assigned 30% of channel 1f to the formation of H_3O^+, supported by our trajectory calculations, as discussed below (see also Table 1).

For the first (1a) dissociation channel, the optimized 0 K appearance energy that provides the best fit to the experimental data was 11.647 ± 0.005 eV, which is only 0.007 eV higher than the calculated value at the aforementioned coupled-cluster level. Furthermore, in order to properly fit the shape of the breakdown curve just before the E_0, the $k(E)$ values of this channel were tripled, compared to the calculated function. Note that if $k(E)$ is very large, it corresponds to a prompt dissociation mechanism, while small $k(E)$ values mean that some of the ions with energy larger than the dissociation threshold do not dissociate during the time it takes for them to reach the detector from the ionization region, blue shifting and broadening slightly the ideal curve corresponding to infinitely fast dissociation. We included this experimental effect explicitly for channel 1a with 2.4 μs characteristic flight time.

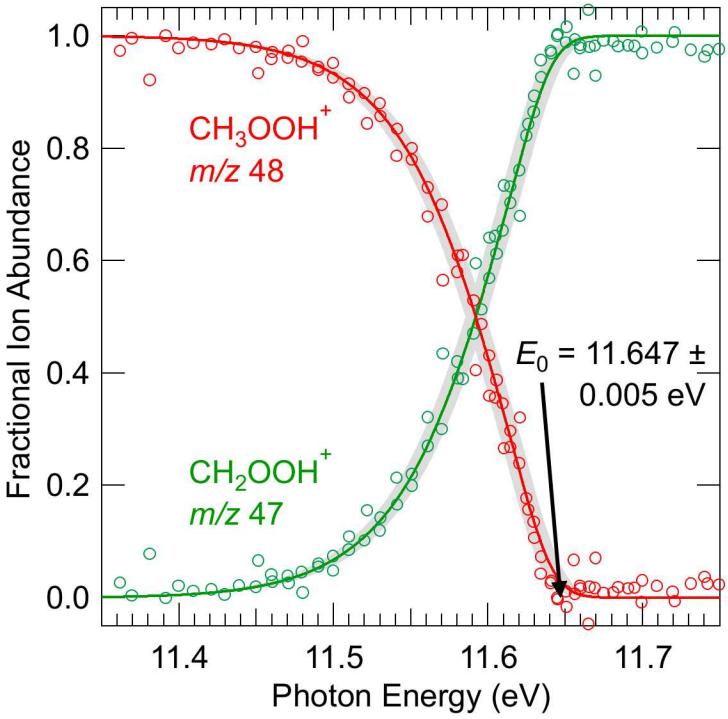

Figure 5. Breakdown diagram of the first dissociation process. Open circles are the experimental fractional ion abundances, solid lines show the results of the RRKM modeling, while the shaded area represents the uncertainties in the 0 K appearance energy.

These RRKM simulations showed that the parent ion is very slightly metastable and taking this into account gives a calculated breakdown curve that is a better fit to the experimental data. However, this "kinetic shift" is miniscule and its only experimental manifestation is a small change in the curvature of the breakdown curve just before the disappearance energy of the CH_3OOH^+ parent ion signal. The best-fit model gives an E_0 of 11.647 ± 0.005 eV and Figure 5 shows the low-energy region of the breakdown curve, with the shaded area representing the confidence interval in the 0 K appearance energy.

The most exothermic product channel, HCO + H_3O^+, is only minor in the experiments, and the model predicts the ion abundances very well if we assume that HCO^+ is the main ion product after the roaming saddle point. To investigate the nature of the main channel after the roaming saddle point (lower red dot in Fig. 3), we ran 100 BOMD trajectory calculations starting at 0.1 and 1 eV above the roaming saddle point. Within the 1000 fs window, only about a third of the trajectories converged, some terminated earlier due to errors, while no reaction happened for others and the ionic complex persisted. As seen in Table 1, approximately 85% of the productive trajectories ended up in H_2O and CH_2O^+ in both cases, or, less frequently, in H_2O + H + HCO^+. In ca. 15% of the cases, the product was H_3O^+ mostly with HCO or, in a few cases, H + CO as neutral fragments. In general, we observed that the fragments stayed together for a relatively long time even in the reactive cases and H atoms transferred back and forth many times before the fragments departed. Although the branching fractions in the BOMD calculations are not quantitative, they nevertheless show that the formation of CH_2O^+ is dominant over H_3O^+. This former ion, however, does not show up in the experimental data, which is explained well by the calculated lifetime of the CH_2O^+ ion after the water molecule leaves. Even if almost all of the excess energy is deposited

into the H_2O neutral co-fragment, the CH_2O^+ ion dissociates in less than a microsecond (*i.e.*, $k(E) > 10^6$ s). At higher energies, the lifetime of CH_2O^+ is orders of magnitudes smaller, which means that CH_2O^+ will readily and completely decompose under the experimental conditions into $HCO^+ + H$. Our model also shows that the yields of HCO^+ via the tight transition states (1f and 1g) are minute. This means that the major source of the $[H_2CO\ldots H_2O]^+$ complex is the roaming rearrangement channel. Further evidence for this proposed mechanism is the excellent agreement between the experimental HCO^+ appearance energy of 12.2 eV with the calculated roaming pathway transition state of 12.19 eV.

The low yield of H_3O^+ in these trajectories can explain the slow rise of trace amounts of the m/z = 19 ion but it cannot be responsible for the sharper rise observed at 13 eV. Notably, at this photon energy, the calculated yield of CH_2OOH^+ starts to deviate from the experimental breakdown curve, the difference gradually reaching 15% at 14 eV. However, if a consecutive dissociation of this H-loss daughter ion is included in the model (equation 7c), calculated from microcanonical product energy distribution functions, as described elsewhere in detail,[45] the experimental and modeled m/z = 47 ion abundance shows almost perfect agreement. The calculated abundance of the H_3O^+ ion, shown with a solid tan line in Figure 1, also agrees reasonably well with the experimental data. Its deviation below 13.2 eV confirms that a minor fraction of this ion is formed in a parallel dissociation of the parent ion, in agreement with the low (but non-zero) H_3O^+ yield in the BOMD simulations.

Table 1. Number of reactive trajectories for the BOMD simulations categorized into various product channels.

channel	0.1 eV excess energy	1.0 eV excess energy
$H_2CO^+ + H_2O$	22	18

$H + HCO^+ + H_2O$	5	10
$HCO + H_3O^+$	3	2
$H + CO + H_3O^+$	1	3
$HCO^+ + H_2 + OH$	1	0
total	32	33
HCO^+ [a]	28 (88%)	28 (85%)
H_3O^+ [b]	4 (12%)	5 (15%)

[a] All channels (eventually) forming HCO^+

[b] All channels forming H_3O^+

4. Thermochemistry

As expected, the most accurate fit of the experimental data was achieved for the primary channel of interest, $CH_3OOH \rightarrow CH_2OOH^+ + H$. The heat of formation for the $QOOH^+$ ion can, therefore, be calculated from the fitted appearance energy of the $QOOH^+$ ion and the heat of formation of MHP:

$$\Delta_f H^\circ_{0\ K}[CH_2OOH^+] = \Delta_f H^\circ_{0\ K}[CH_3OOH] - \Delta_f H^\circ_{0\ K}[H] + E_0$$

As shown also in Figure 5, the E_0 obtained by fitting the RRKM model to the experimental breakdown curve is 11.647 ± 0.005 eV (1123.8 ± 0.5 kJ mol^{-1}). Using 216.034 ± 0.000 kJ mol^{-1} for $\Delta_f H^\circ_{0\ K}$ [H] and –114.90 ± 0.74 kJ mol^{-1} for $\Delta_f H^\circ_{0\ K}$ [CH_3OOH] from the Active Thermochemical Tables[11] gives a gas-phase 0 K heat of formation of 792.8 ± 0.9 kJ mol^{-1} for the CH_2OOH^+ ion. In order to calculate a mixed experimental-theoretical value for the CH_2OOH radical's heat of formation, we have obtained its ionization energy to be 718.59 kJ mol^{-1} at the F12//M06-2X level. Using this calculated value with a reasonable error estimate of ± 2.4 kJ mol^{-1} (25 meV), the 0 K heat of formation for the CH_2OOH radical was found to be 74.2 ± 2.6 kJ mol^{-1}. For comparison, using the ATcT value of the MHP heat of formation, but the calculated ZPE-

corrected energies of MHP, CH_2OOH, and H at the F12//M06-2X level, the 0 K heat of formation of CH_2OOH is 73.6 kJ mol^{-1}.

The proton affinity of one of the Holy Grails of atmospheric chemistry, the CH_2OO Criegee intermediate,[46, 47] can also be directly obtained using our heat of formation of CH_2OOH^+ combined with the ATcT recommended $\Delta_f H^e_{0\ K}$ [CH_2OO] of 112.43 ± 0.61 kJ mol^{-1} and $\Delta_f H^e_{0\ K}$ [H^+] of 1528.084 ± 0.000 kJ mol^{-1}. The CH_2OO proton affinity of 847.7 ± 1.1 kJ mol^{-1} is in agreement with the 850.6 ± 4.2 kJ mol^{-1} (203.3 ± 1.0 kcal mol^{-1}) from CCSD(T)/CBS calculations by Nguyen *et al*.[48] and reduces its uncertainty by a factor of 4.

Conclusions

The dissociative photoionization of methyl hydroperoxide has been studied by imaging PEPICO experiments and extensive quantum-chemical and statistical rate calculations. A remarkable agreement has been achieved between the measured and modeled breakdown diagrams by adjusting just a few model parameters. Experimentally, MHP has been found to dissociate primarily into CH_2OOH^+ (the simplest $QOOH^+$ ion), HCO^+, H_3O^+, and CH_3^+ ion within a photon energy range of 11.4–14.0 eV. According to theory, CH_2OOH^+ and CH_3^+ are both formed by a simple bond scission, with only a small reverse barrier for the former channel. Since the CH_2OOH^+ daughter ion represents the ionized form of the corresponding QOOH radical, its thermochemistry is of considerable interest. As expected, this ion is the first dissociation product, with no overlap with other fragments and modeling this dissociation channel gave its appearance energy with sub-kJmol^{-1} accuracy. Using the appearance energy of the $QOOH^+$ ion and the calculated ionization energy of the QOOH radical, a mixed experimental-theoretical heat of formation of 74.5 ± 2.6 kJ

mol^{-1} was obtained for the CH_2OOH radical. As a corollary, a proton affinity of 847.7 ± 1.1 kJ mol^{-1} was also obtained for the smallest Criegee intermediate, CH_2OO.

The HCO^+ fragment ion, which dominates the high-energy portion of the breakdown curve, was found to be produced by a non-statistical process, through a roaming transition state. Due to the dynamic nature of the roaming rearrangement process leading to the $[CH_2O…H_2O]^+$ complex and its fragmentation, H_3O^+ formation represents only a minor channel from the MHP molecular ion. Direct dynamics simulations have shown that the roaming transition state almost always leads to the entropically more favored loss of water, effectively shutting out H_3O^+ formation. Then, in a consecutive process, the HCO^+ ion forms through a fast dissociation of an H atom from the energized H_2CO^+ species. At higher energies, however, H_3O^+ appears with a steep rise in the breakdown curve and its formation is confirmed to proceed from the CH_2OOH^+ fragment ion, though a likely OH-roaming transition state. Together with the aforementioned direct C–O fission of the molecular ion leading to the methyl cation, the theoretical dissociation pathways show excellent agreement with the experimental data and a full RRKM modeling based on the proposed mechanism needed only small tuning to match the experimental ion abundances. From this model, the HCO^+ and H_3O^+ appearance energies were determined to be 12.15 ± 0.05 eV and 13.1 ± 0.1 eV, respectively, while the calculated $E_0(CH_3^+)$ of 12.73 eV did not need to be adjusted to fit the model.

Conflicts of Interest

There are no conflicts to declare.

Acknowledgements

This work has been funded by the National Science Foundation (Grant No. CHE-1665464) and by the Swiss Federal Office for Energy (BFE Contract No. SI/501269-01). JZ was funded under DOE BES, the Division of Chemical Sciences, Geosciences, and Biosciences. Sandia National Laboratories is a multimission laboratory managed and operated by National Technology and Engineering Solutions of Sandia, LLC., a wholly owned subsidiary of Honeywell International, Inc., for the U.S. Department of Energy's National Nuclear Security Administration under contract DE-NA0003525, and this fund allowed her to carry out the quantum chemical and statistical calculations. The views expressed in the article do not necessarily represent the views of the U.S. Department of Energy or the United States Government.

Notes and References

1. J. Zádor, C. A. Taatjes and R. X. Fernandes, *Prog. Energy Combust. Sci.*, 2011, **37**, 371.

2. A. W. Jasper, S. J. Klippenstein and L. B. Harding, *Proc. Combust. Inst.*, 2009, **32**, 279.

3. A. V. Jackson, *Crit. Rev. Environ. Sci. Technol.*, 1999, **29**, 175.

4. C. M. Roehl, Z. Marka, J. L. Fry and P. O. Wennberg, *Atmos. Chem. Phys.*, 2007, **7**, 713.

5. G. L. Vaghjiani and A. R. Ravishankara, *J. Phys. Chem.*, 1989, **93**, 1948.

6. F.-Y. Liu, Z.-W. Long, X.-F. Tan and B. Long, *Comput. Theor. Chem.*, 2014, **1038**, 33.

7. J. Zádor, H. Huang, O. Welz, J. Zetterberg, D. L. Osborn and C. A. Taatjes, *Phys. Chem. Chem. Phys.*, 2013, **15**, 10753.

8. J. D. Savee, E. Papajak, B. Rotavera, H. Huang, A. J. Eskola, O. Welz, L. Sheps, C. A. Taatjes, J. Zádor and D. L. Osborn, *Science*, 2015, **347**, 643.

9. J. Matthews, A. Sinha and J. S. Francisco, *J. Chem. Phys.*, 2005, **122**, 221101.

10. S. L. Khursan and V. Martemyanov, *Russ. J. Phys. Chem. A*, 1991, **65**, 321.

11. B. Ruscic and D. H. Bross, Active Thermochemical Tables (ATcT) values based on ver. 1.122 of the Thermochemical Network (2016); available at ATcT.anl.gov (accessed April 4, 2018).

12. L. Yi-Min, S. Qiao, L. Hai-Yang, G. Mao-Fa and W. Dian-Xun, *Chin. J. Chem.*, 2005, **23**, 993.

13. M. Aschi, M. Attina, F. Cacace, R. Cipollini and F. Pepi, *Inorg. Chim. Acta*, 1998, **276**, 192.

14. C. A. Schalley, D. Schroder and H. Schwarz, *Int. J. Mass Spectrom. Ion Proc.*, 1996, **153**, 173.

15. K. Voronova, K. M. Ervin, K. G. Torma, P. Hemberger, A. Bodi, T. Gerber, D. L. Osborn and B. Sztáray, *J. Phys. Chem. Lett.*, 2018, **9**, 534.

16. G. A. Garcia, B. Gans, J. Kruger, F. Holzmeier, A. Roder, A. Lopes, C. Fittschen, C. Alcaraz and J.-C. Loison, *Phys. Chem. Chem. Phys.*, 2018, **20**, 8707.

17. K. Voronova, C. M. Mozaffari Easter, K. G. Torma, A. Bodi, P. Hemberger and B. Sztáray, *Phys. Chem. Chem. Phys.*, 2016, **18**, 25161.

18. X. Tang, X. Lin, W. Zhang, G. A. Garcia and L. Nahon, *Phys. Chem. Chem. Phys.*, 2016, **18**, 23923.

19. A. Bodi, J. Csontos, M. Kállay, S. Borkar and B. Sztáray, *Chem. Sci.*, 2014, **5**, 3057.

20. A. Bodi, B. Sztáray and T. Baer, *Phys. Chem. Chem. Phys.*, 2006, **8**, 613.

21. D. W. Osullivan, M. Y. Lee, B. C. Noone and B. G. Heikes, *J. Phys. Chem.*, 1996, **100**, 3241.

22. M. Johnson, A. Bodi, L. Schulz and T. Gerber, *Nucl. Instrum. Methods Phys. Res., Sect. A*, 2009, **610**, 597.

23. A. Bodi, M. Johnson, T. Gerber, Z. Gengeliczki, B. Sztáray and T. Baer, *Rev. Sci. Instrum.*, 2009, **80**, 034101.

24. W. C. Wiley and I. H. McLaren, *Rev. Sci. Instrum.*, 1955, **26**, 1150.

25. A. Bodi, B. Sztáray, T. Baer, M. Johnson and T. Gerber, *Rev. Sci. Instrum.*, 2007, **78**, 084102.

26. J. C. Poully, J. P. Schermann, N. Nieuwjaer, F. Lecomte, G. Gregoire, C. Desfrançois, G. A. Garcia, L. Nahon, D. Nandi and L. Poisson, *Phys. Chem. Chem. Phys.*, 2010, **12**, 3566.

27. A. Bodi, P. Hemberger and R. P. Tuckett, *Phys. Chem. Chem. Phys.*, 2017, **19**, 30173.

28. A. Bodi and P. Hemberger, *Phys. Chem. Chem. Phys.*, 2014, **16**, 505.

29. B. Sztáray and T. Baer, *Rev. Sci. Instrum.*, 2003, **74**, 3763.

30. M. J. Frisch, G. W. Trucks, H. B. Schlegel, G. E. Scuseria, M. A. Robb, J. R. Cheeseman, G. Scalmani, V. Barone, B. Mennucci, G. A. Petersson, H. Nakatsuji, M. Caricato, X. Li, H. P. Hratchian, A. F. Izmaylov, J. Bloino, G. Zheng, J. L. Sonnenberg, M. Hada, M. Ehara, K. Toyota, R. Fukuda, J. Hasegawa, M. Ishida, T. Nakajima, Y. Honda, O. Kitao, H. Nakai, T. Vreven, J. Montgomery, J. A., J. E. Peralta, F. Ogliaro, M. Bearpark, J. J. Heyd, E. Brothers, K. N. Kudin, V. N. Staroverov, R. Kobayashi, J. Normand, K. Raghavachari, A. Rendell, J. C. Burant, S. S. Iyengar, J. Tomasi, M. Cossi, N. Rega, N. J. Millam, M. Klene, J. E. Knox, J. B. Cross, V. Bakken, C. Adamo, J. Jaramillo, R. Gomperts, R. E. Stratmann, O. Yazyev, A. J. Austin, R. Cammi, C. Pomelli, J. W. Ochterski, R. L. Martin, K. Morokuma, V. G. Zakrzewski, G. A. Voth, P. Salvador, J. J. Dannenberg, S. Dapprich, A. D. Daniels, Ö. Farkas, J. B. Foresman, J. V. Ortiz, J. Cioslowski and D. J. Fox, *Gaussian 09, Revision A.02*, Gaussian, Inc., Wallingford CT, 2009.

31. H. J. Werner, P. J. Knowles, G. Knizia, F. R. Manby and M. Schutz, *Wiley Interdiscip. Rev. Comput. Mol. Sci.*, 2012, **2**, 242.

32. T. J. Lee, A. P. Rendell and P. R. Taylor, *J. Phys. Chem.*, 1990, **94**, 5463.

33. T. J. Lee and P. R. Taylor, *Int. J. Quant. Chem.*, 1989, **S23**, 199.

34. Y. Georgievskii, J. A. Miller, M. P. Burke and S. J. Klippenstein, *J. Phys. Chem. A.*, 2013, **117**, 12146.

35. Y. Georgievskii and S. J. Klippenstein, *J. Phys. Chem. A.*, 2003, **107**, 9776.

36. Y. Georgievskii and S. J. Klippenstein, *J. Chem. Phys.*, 2003, **118**, 5442.

37. Y. Georgievskii and S. J. Klippenstein, VaReCoF, Sandia National Laboratories and Argonne National Laboratory, 2006.

38. T. Baer and W. L. Hase, *Unimolecular Reaction Dynamics: Theory and Experiments*, Oxford University Press on Demand, New York, 1996.

39. J. D. Lewis, T. B. Malloy, T. H. Chao and J. Laane, *J. Mol. Struct.*, 1972, **12**, 427.

40. E. M. Russell, E. Cudjoe, M. E. Mastromatteo, J. P. Kercher, B. Sztáray and A. Bodi, *J. Phys. Chem. A.*, 2013, **117**, 4556.

41. C. A. Grambow, A. Jamal, Y.-P. Li, W. H. Green, J. Zádor and Y. V. Suleimanov, *J. Am. Chem. Soc.*, 2018, **140**, 1035.

42. O. Welz, S. J. Klippenstein, L. B. Harding, C. A. Taatjes and J. Zádor, *J. Phys. Chem. Lett.*, 2013, **4**, 350.

43. W. H. Miller, *J. Chem. Phys.*, 1976, **65**, 2216.

44. J. Zádor, A. W. Jasper and J. A. Miller, *Phys. Chem. Chem. Phys.*, 2009, **11**, 11040.

45. B. Sztáray, A. Bodi and T. Baer, *J. Mass Spectrom.*, 2010, **45**, 1233.

46. O. Welz, J. D. Savee, D. L. Osborn, S. S. Vasu, C. J. Percival, D. E. Shallcross and C. A. Taatjes, *Science*, 2012, **335**, 204.

47. L. Sheps, B. Rotavera, A. J. Eskola, D. L. Osborn, C. A. Taatjes, K. Au, D. E. Shallcross, M. A. H. Khan and C. J. Percival, *Phys. Chem. Chem. Phys.*, 2017, **19**, 21970.

48. M. T. Nguyen, T. L. Nguyen, V. T. Ngan and H. M. T. Nguyen, *Chem. Phys. Lett.*, 2007, **448**, 183.